

Effects of the container on structure function with impedance map analysis of dense scattering media

Adam C. Luchies and Michael L. Oelze

Beckman Institute for Advanced Science and Technology, Department of Electrical and Computer Engineering, University of Illinois at Urbana-Champaign, 405 North Mathews Avenue, Urbana, Illinois 61802, USA

(Received 29 November 2017; revised 20 February 2018; accepted 13 March 2018; published online 18 April 2018)

Quantitative ultrasound (QUS) can be used to estimate acoustic properties of tissue microstructure. In one approach to QUS, the backscatter coefficient (BSC) is utilized to quantify and classify tissue state. From the BSC, parametric models can be constructed to relate the frequency-dependent BSC to geometrical properties of the underlying tissue. However, most of these parametric models are based on analytic expressions (e.g., Gaussian function) and not on actual tissue morphology. Impedance map analysis has been proposed to help identify sources of ultrasonic scattering in tissues and to develop improved models of scattering. Previously, two-dimensional impedance maps (2DZMs) were demonstrated to provide tissue models of three-dimensional (3D) structures for sparse scattering media. In the current study, 2DZMs analysis of dense scatterer media combining the structure function with impedance map analysis was studied through a series of simulations. The simulation analysis demonstrated that the correlation coefficient and power spectrum could be estimated for a dense collection of spheres using 2DZMs. The current finding implies that 2DZMs can capture information about the 3D spatial positions of scatterers in addition to information about the size and shape of the scatterers for a dense scattering media, which is expected to be encountered in many tissues. © 2018 Acoustical Society of America. <https://doi.org/10.1121/1.5031124>

[GH]

Pages: 2172–2181

I. INTRODUCTION

Ultrasound imaging has achieved widespread use for internal imaging of the human body over the past several decades. The following characteristics of the ultrasound imaging modality have contributed to its success: ultrasound images can be formed in real-time, ultrasound machines are inexpensive and can be made to be portable, and ultrasound uses non-ionizing radiation. Future technological development of ultrasound image processing techniques will continue to expand its use in diagnostic and therapy monitoring applications.

Conventional diagnostic ultrasonic imaging is focused on the construction of B-mode images from ultrasonic backscatter to depict anatomical structures in patients. However, these B-mode images are highly qualitative and the quantitative information in these images is reduced due to the processing of the raw backscatter data. Typically, a B-mode image is constructed by detecting the envelope of the backscattered signal, compressing the envelope via a decibel scale and displaying the image in grayscale as a function of intensity. The envelope detection results in discarding of the frequency-dependent information inherent in the backscattered signal.

The goal of spectral-based quantitative ultrasound (QUS) imaging approaches is to utilize the raw backscattered signals to infer characteristics of the underlying tissues through analysis of the frequency-dependent information in the signals. Normally, spectral-based methods make use of the backscatter coefficient (BSC) to characterize tissue state or identity. For example, QUS methods based on estimating the backscatter coefficient (BSC) have been used in the eye (Feleppa *et al.*, 1986), prostate (Feleppa *et al.*, 1996), heart

(Tamirisa *et al.*, 2001), kidney (Insana, 1995), liver (Fellingham and Sommer, 1984), breast (Oelze *et al.*, 2004), cancerous lymph nodes (Mamou *et al.*, 2011), monitoring cell death (Czarnota *et al.*, 1999), and evaluating disease treatment (Vlad *et al.*, 2009).

The BSC is defined as the differential backscattering cross section divided by unit volume of the scattering region. As such, the BSC is a fundamental property of a tissue, much like sound speed and attenuation, and can be used to uniquely identify several tissues. The BSC is based on the frequency power spectrum estimated from the radio frequency (RF) signals corresponding to ultrasonic backscatter. Traditionally, to characterize tissue based on the spectral features of the backscattered signal, models of the tissue scattering are utilized to parameterize the frequency dependence of the BSC. From the BSC, form factor models can be constructed to relate the frequency-dependent BSC to geometrical properties of the underlying tissue. Feature extraction is performed on the form factor using parametric models and the estimated parameters used in a classification task for the case of disease diagnosis or in a regression task for the case of therapy monitoring.

The BSC modeling problem is fundamentally ill-posed because an infinite number of models could be designed to capture the frequency-dependent behavior of the BSC (e.g., splines). Therefore, the model space is usually constrained to parametric models derived from scatterer geometries such as the fluid-filled sphere (Anderson, 1950), spherical shell (Insana *et al.*, 1990), two concentric spheres (McNew *et al.*, 2009), etc. Using these models, acoustic properties related to

tissue microstructure such as the effective scatterer diameter (ESD) and the effective acoustic concentration (EAC) can be estimated.

When examining complex biological tissues, constraining the model space in the described manner can be a major deficiency. Failure modes include the existence of large errors between the actual and modeled BSC or histological observation that does not agree with the estimated ESD and EAC. In addition, the BSC is usually estimated for a finite frequency range, so different parametric models may fit the BSC equally well while providing different parameter estimates. It is clear that improved methods are needed for feature extraction that agree with histological observation and that reduce error between actual and modeled BSC.

The primary goal of impedance map (ZM) analysis is to use maps of acoustic properties created using optical or scanning acoustic microscopy to study the BSC and either help identify sources of scattering in tissues or develop new models based on tissue structure directly (Ueda and Ozawa, 1985; Insana *et al.*, 1990; Chen *et al.*, 1997; Mamou *et al.*, 2008; Lavarello *et al.*, 2011). ZM analysis relies on the theory of weak acoustic scattering by plane waves, which has been described previously by Morse and Ingard (1968), Insana *et al.* (1990), and Insana and Brown (1992). Based on these descriptions of weak scattering theory, Mamou *et al.* (2005) developed procedures for utilizing three-dimensional impedance maps (3DZMs) to predict ultrasonic scattering from biological tissues, i.e., the three-dimensional (3D) volume power spectrum of the 3DZM was directly related to the BSC.

Procedures for creating 3DZMs include utilizing a series of adjacent histological tissue slides that have been stained to emphasize acoustic impedance structures. The serial histological slides are digitized using a camera, serial slides are aligned and registered spatially to form a 3D matrix, and each pixel in the matrix is assigned an impedance value based on color thresholds. In the case of an isotropic medium, the 3D power spectrum of the 3DZM can be radially averaged and related to the power spectrum of the ultrasound backscatter signal (Luchies and Oelze, 2016). This reduces the noise inherent in the power spectrum estimates for a single 3DZM. If the medium is anisotropic, to estimate the power spectrum associated with the backscatter, the ultrasound propagation direction must be known relative to the orientation of the 3DZM. The power spectrum corresponding to the k -space line of the 3DZM power spectrum parallel to the ultrasound propagation direction can be extracted but cannot be averaged over many different angles, resulting in a much noisier estimate of the power spectrum for a single 3DZM block.

In a previous study, we examined the use of two-dimensional impedance maps (2DZMs) to provide estimates of the power spectrum from tissue structures (Luchies and Oelze, 2016). The rationale for the use of 2DZMs as opposed to 3DZMs is the time associated with slide preparation, computational time associated with the registration and estimation process and the financial costs associated with production of many serial tissue slides. Misregistration of slides in the 3DZM, missing slide sections, and difference in the amount of stain taken up by slides in the 3D block result

in poorer performance of the model estimation from 3DZMs. Furthermore, to obtain good estimates, it is often necessary to average power spectral estimates from several 3DZM blocks.

On the other hand, 2DZMs do not need registration, the costs associated with their production is much lower, and averaging from many independent 2DZMs is possible. 2DZMs are not subject to these same constraints as the 3DZMs but do suffer from different tradeoffs. For example, 2DZMs must assume isotropy or weak anisotropy (Luchies, 2016). Second, previous 2DZM analysis was demonstrated to work only with sparse scattering, i.e., a low concentration of scatterers.

In this work, we extend the utilization of 2DZMs to account for a dense population of scatterers. We first describe scattering from a dense population of scatterers and how this affects a ZM analysis. Simulations are then utilized to quantify the ability of 2DZMs to account for dense populations of scatterers when confined within a container. We end with a discussion of the important features of 2DZM analysis in the context of a dense scattering medium.

II. THEORY

We first consider a medium having a background with compressibility and density given by κ_0 and ρ_0 , respectively. Scattering in the medium can occur if an inhomogeneity exists with compressibility and density values that are different from the background. If plane wave propagation of ultrasound is assumed in a medium with weak scattering and spatially random variations in compressibility and density, i.e., impedance, then the BSC can be described by (Insana and Brown, 1992)

$$\sigma_b = \frac{k^4 \langle \gamma^2 \rangle}{16\pi^2} \int_{-\infty}^{\infty} b_\gamma(\Delta \mathbf{r}) \exp(-j2k\hat{\mathbf{o}} \cdot \Delta \mathbf{r}) d^3 \Delta \mathbf{r}, \quad (1)$$

where k is the wavenumber, $\Delta \mathbf{r} = \mathbf{r}_1 - \mathbf{r}_2$ is the lag vector, $\hat{\mathbf{o}}$ points in the direction of the backscattered wave, $b_\gamma(\Delta \mathbf{r})$ is the correlation coefficient of the spatially varying impedance, γ , with

$$\gamma(\mathbf{r}) \approx -2 \frac{z(\mathbf{r}) - z_0}{z_0}. \quad (2)$$

Equation (1) indicates that the BSC is related to the 3D Fourier transform of the 3D correlation coefficient of the impedance distribution in the scattering volume. Therefore, the BSC can be estimated from the correlation coefficient, which can be calculated directly from the 3DZM. If the medium is isotropic, or weakly anisotropic (Luchies, 2016), a 2DZM can be used to estimate the BSC because $b_\gamma(\Delta \mathbf{r})$ is radially symmetric and the BSC reduces to

$$\sigma_b = \frac{k^3 \langle \gamma^2 \rangle}{8\pi} \int_0^{\infty} b_\gamma(\Delta r) \sin(2k\Delta r) \Delta r d\Delta r. \quad (3)$$

The same type of modeling is possible when estimating the BSC using ultrasound, so parameters using ZMs and ultrasound can be compared. When performing this type of modeling, it is necessary to assume that the positions of the

inhomogeneities are uncorrelated; otherwise a structure factor (Twersky, 1987), will distort the shape of the estimated correlation coefficient and power spectrum using ZMs and the shape of the BSC estimated using ultrasound, leading to errors in the scatterer size estimates.

The development so far has assumed that the scatterer positions are independent. When this assumption fails, a structure function must be added to the BSC to account for the correlations between scatterer positions. Structure functions have been used previously in modeling backscatter from red blood cells (Fontaine *et al.*, 1999; Franceschini *et al.*, 2010; Franceschini *et al.*, 2011) and biophantoms (Han and O'Brien, 2015). For a collection of monodisperse scatterers, the structure function is defined as

$$S(\mathbf{k}) = 1 + \bar{n} \int_{-\infty}^{\infty} [g(\Delta\mathbf{r}) - 1] e^{-j\mathbf{k}\cdot\Delta\mathbf{r}} d^3\Delta\mathbf{r}, \quad (4)$$

where \bar{n} is the number density of scatterers and $g(\Delta\mathbf{r})$ is the pair correlation function governing the spatial distribution of the scatterers. The pair correlation function is a statistical quantity that is proportional to the probability of finding a second scatterer at a position $\Delta\mathbf{r}$ relative to a first scatterer.

The independent positions (IP) pair correlation function is given by

$$g_{IP}(\Delta r) = 1. \quad (5)$$

The hole-correction (HC) approximation is a better model for non-overlapping scatterers that enforces a minimal separation between the scatterers

$$g_{HC}(\Delta r) = \begin{cases} 0, & \Delta r \leq 2a \\ 1, & \Delta r > 2a, \end{cases} \quad (6)$$

where a is the radius of the scatterer. The HC approximation gives a reasonable description of sparsely packed scatterers, but breaks down for dense packings. For a collection of non-overlapping monodisperse spheres, the Percus-Yevick (PY) approximation is frequently used to solve the Ornstein-Zernike (OZ) equation for the PY pair correlation function $g_{PY}(\Delta r)$ (Percus and Yevick, 1958). Examples of pair correlation functions are provided in Fig. 1.

To account for the structure function, the BSC is written as

$$\sigma_b = \sigma_0 FF(2k)S(2k), \quad (7)$$

where σ_0 is the BSC for a point scatterer and FF is the form factor, which is derived from the ZM analysis. Examples of the fluid sphere model form factor multiplied by the PY structure function are shown in Fig. 2. These examples demonstrate the significant effect that the structure function can have on the shape of the scattering amplitude. These shape changes produce errors in size estimates when modeling power spectra from ZMs or BSCs estimated using ultrasound.

ZMs are confined to a finite volume called a container. This container will primarily affect the estimated power spectrum and parameters estimated using the power spectrum. Therefore, it is important to predict the effects that the container will have on estimation procedures (Luchies and Oelze, 2013).

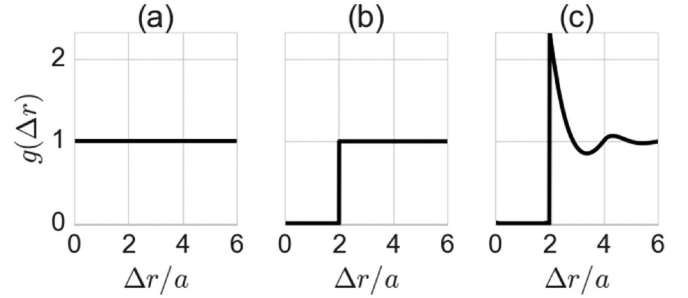


FIG. 1. Pair correlation function assuming (a) IP, (b) hole-corrections approximation, and (c) PY approximation.

Associated with a container are its shape (e.g., cube, sphere, cylinder, etc.) and its size (characteristic dimension of the container such as side length or diameter). The probability distribution for the scatterer positions is affected by the size and shape of a container. Therefore, a structure function was developed that included the effects of the container and a specified pair correlation function.

A finite collection of monodisperse scatterers in n -dimensions may be described mathematically in the following way. A single scatterer centered at the origin is denoted by $h(\mathbf{r})$. The spatial positions of each scatterer are given by

$$s(\mathbf{r}) = \frac{1}{N} \sum_{n=1}^N \delta(\mathbf{r} - \mathbf{r}_n), \quad (8)$$

where δ is the Dirac delta function, N is the total number of scatterers in the collection, and \mathbf{r}_n records the position of the n th scatterer. The collection of scatterers is written as

$$f(\mathbf{r}) = N \cdot [h * s], \quad (9)$$

where $*$ indicates spatial convolution. The volume power spectrum for the collection of scatterers is given by

$$F(\mathbf{k}) = N[H(\mathbf{k}) \cdot S(\mathbf{k})], \quad (10)$$

where \mathbf{k} is the wavenumber vector, $S(\mathbf{k})$ is the power spectrum of $s(\mathbf{r})$, and $H(\mathbf{k})$ is the power spectrum of $h(\mathbf{r})$. $S(\mathbf{k})$ is the structure function

$$S(\mathbf{k}) = \frac{1}{N} \left| \sum_{m=1}^N e^{-j\mathbf{k}\cdot\mathbf{r}_m} \right|^2 = 1 + \frac{1}{N} \sum_{m \neq n} \cos(\mathbf{k} \cdot \Delta\mathbf{r}_{m,n}), \quad (11)$$

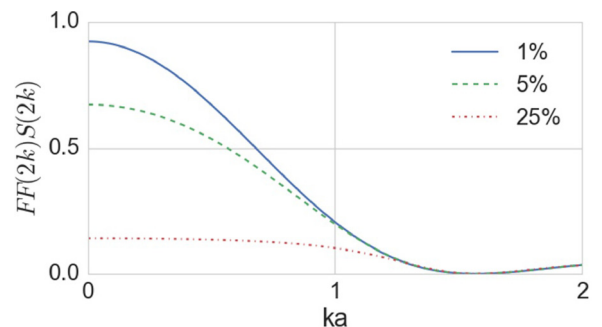


FIG. 2. (Color online) Examples of the fluid sphere form factor multiplied by the PY structure function (blue) 1%, (green) 5%, and (red) 25% volume fractions.

where $\Delta\mathbf{r}_{m,n} = \mathbf{r}_n - \mathbf{r}_m$ is the spacing vector between the m th and n th scatterers. The first addend in Eq. (11) is called the incoherent component because it does not depend on $\Delta\mathbf{r}_{m,n}$. The second addend in Eq. (11) is called the coherent component because it does depend on $\Delta\mathbf{r}_{m,n}$, i.e., the spatial positions of the scatterers relative to each other determine the magnitude of this term.

If the scatterer positions are known, the structure function can be computed directly from Eq. (11). If the scatterer positions are unknown, the expected value for the structure function can be found from the probability distribution of the scatterer spacings, assuming a random spatial distribution. The expected value of the structure function is given as

$$E[S(\mathbf{k})] = 1 + (N - 1) \int_{-\infty}^{\infty} p(\Delta\mathbf{r}) \cos(\mathbf{k} \cdot \Delta\mathbf{r}) d^n \Delta\mathbf{r}, \quad (12)$$

where $p(\Delta\mathbf{r})$ is the probability distribution function and the integral is over an n -dimensional space.

For independent scatterer positions confined to a container, which is the case for a ZM analysis, small spacings are more likely to occur than large spacings. Therefore, in 3D for a cube container, it is reasonable to assume that the scatterer spacings will follow a triangle distribution along one dimension. It should be noted that a triangle function results when a rectangular function is convolved with itself.

Let an n -dimensional container be specified by $w(\mathbf{r})$. For example, a cube container in 3D with sidelength L and centered at the origin can be written as

$$w_{cube}(\mathbf{r}) = \text{rect}\left(\frac{x}{L}\right) \text{rect}\left(\frac{y}{L}\right) \text{rect}\left(\frac{z}{L}\right), \quad (13)$$

where $\text{rect}(x/L)$ is a rectangular function centered at the origin and having a width L . A sphere in 3D with a diameter L and centered at the origin can be written as

$$w_{sphere}(\mathbf{r}) = \text{sphere}\left(\frac{r}{L}\right). \quad (14)$$

The spatial autocorrelation function of a container $w(\mathbf{r})$ is defined as $W(\Delta\mathbf{r}) = w(\mathbf{r}) * w(-\mathbf{r})$. It is a straightforward exercise to derive the autocorrelation functions for both of these containers. The proposed model for the scatterer spacing probability distribution assuming a container with autocorrelation function $W(\Delta\mathbf{r})$ and pair correlation function $g(\Delta\mathbf{r})$ is defined as

$$p(\Delta\mathbf{r}) = \frac{g(\Delta\mathbf{r})W(\Delta\mathbf{r})}{\int g(\Delta\mathbf{r})W(\Delta\mathbf{r})d^n \Delta\mathbf{r}}. \quad (15)$$

This function satisfies the properties required for a probability distribution and incorporates the pair correlation function of the scatterers and the size and shape the container. Examples of cross sections from 3D scatterer spacing probability distributions are shown in Fig. 3 for different containers and different pair correlation functions.

In the case of IP, analytic forms of the structure function for the cube and sphere containers can be found. For the

cube container with sidelength L , the structure function takes the form

$$S(\mathbf{k}) = 1 + (N - 1) \times \left[\text{sinc}^2\left(\frac{k_x L}{2}\right) \text{sinc}^2\left(\frac{k_y L}{2}\right) \text{sinc}^2\left(\frac{k_z L}{2}\right) \right]. \quad (16)$$

For the sphere container with diameter L , the structure function takes the form

$$S(\mathbf{k}) = 1 + (N - 1) \left[3 \frac{j_1\left(\frac{kL}{2}\right)}{\frac{kL}{2}} \right]^2. \quad (17)$$

Radial lines from the IP structure function for a cube container are shown in Fig. 4, which are included to illustrate the shape of a structure function due to container effects. This structure function displays a large peak centered at $ka=0$. This peak results because the cosine function approaches one as ka goes to zero, causing the structure function to approach N . The width of this large peak is controlled by the container size. The structure function assuming IP and a sphere container is shown in Fig. 5. It should be noted that the structure function for the cube container is not radially symmetric while the structure function for the sphere container is radially symmetric. Thus, when using a

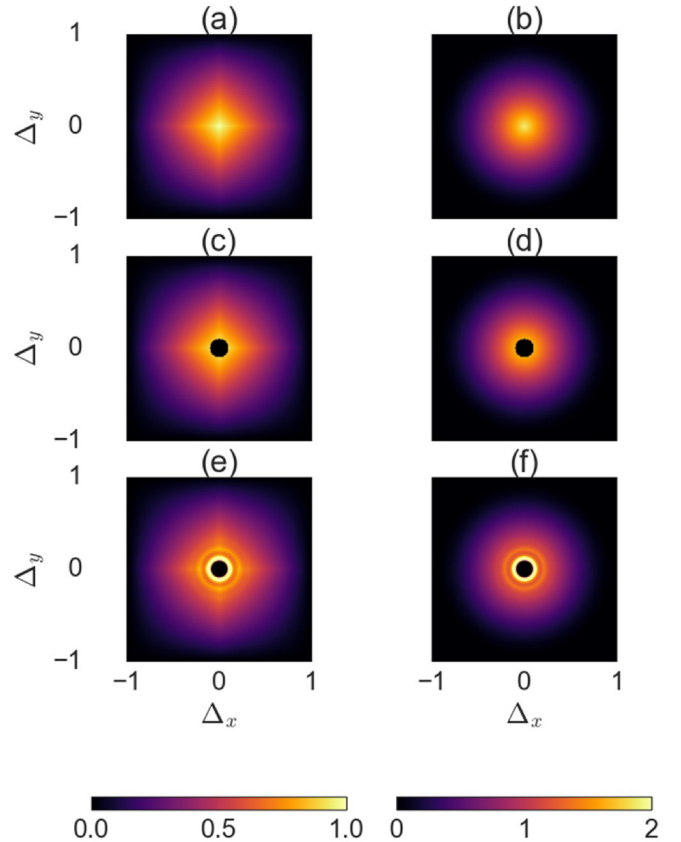


FIG. 3. (Color online) Example cross sections from scatterer spacing probability distribution $p(\Delta\mathbf{r})$. Assuming (a), (c), (e) cube container and (b), (d), (f) sphere container. Assuming (a), (b) IP, (c), (d) HC approximation and (e), (f) PY pair approximation. The container length was equal to 1.0 and the spheres had radius 0.05.

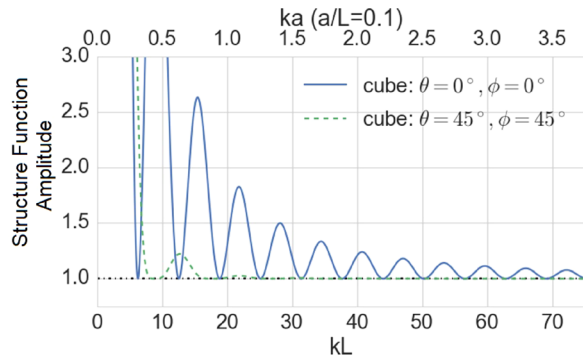


FIG. 4. (Color online) Example structure functions (unitless) assuming IP and a cube container. A total of 100 scatterers were in the container and the ratio of the scatterer radius to the container dimension was $a/L=0.1$. Two polar/azimuthal angle combinations are shown.

cube container, radial averaging is not appropriate and a different container such as a sphere should be used or off-axis radial lines should be analyzed.

Examples of structure functions for a spherical container and assuming the PY pair correlation function are shown in Fig. 6, i.e., the spacing probability distribution shown in Fig. 3(f) was used. As the container becomes large compared to the scatterer size, the expected behavior was that the structure function with container effects would converge to the PY structure function. The results in Fig. 6 show that the structure function model with container followed this behavior.

The largest deviations between the PY structure function and structure function with container were observed for the largest volume fraction. In particular, when the ratio between the scatterer size and container dimension was 0.3 and the volume fraction was 50%, i.e., the blue curve in Fig. 6(c), significant discrepancies were observed between the PY structure function and the structure function with container effects. For this volume fraction, the PY structure function displayed a large peak in the range $1.5 \leq ka \leq 2$. In contrast, the PY structure function with a container reduced the magnitude of this peak as this structure function was approaching one, i.e., the IP structure function. This behavior can be explained because the container has the effect of filtering the PY pair correlation function shown in Fig. 1(c).

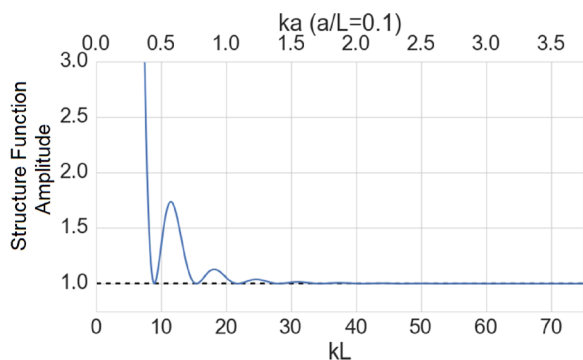


FIG. 5. (Color online) Example structure function (unitless) assuming IP and a spherical container. A total of 100 scatterers were in the container and the ratio of the scatterer radius to the container dimension was $a/L=0.1$. The function is radially symmetric.

When a container is introduced, the large r content in the PY pair correlation function is reduced in magnitude or eliminated, thus reducing its effect on the structure function and causing the structure function with container to not display large peaks similar to the PY structure function.

Similar to the IP structure function for a sphere container, the PY structure function with container displayed a large peak centered at $ka=0$. The width of this peak was controlled by the size of the container relative to the scatterer size. As the container was made larger, the width of this peak decreased, and as the container was made smaller, the width of this peak increased. Making the container large enough so that this large peak does not affect the ka range of interest is an important consideration when determining container size relative to the scatterer size. Based on Fig. 6, the ratio between scatterer radius and container length ($a=L$) should be less than 0.1 to prevent this main peak from affecting the range $ka > 0.5$.

III. SIMULATION

Simulations were constructed by placing spheres of select size distributions in a container to achieve a specified volume fraction and test the above theoretical predictions. In order to provide a dense scattering medium for simulation, the Metropolis algorithm was utilized (Widom, 1966). This algorithm results in a maximum achievable volume fraction of approximately 64% in 3D for monodisperse spheres.

A. Structure function versus container model

The first set of simulations was used to test the structure function versus container model. Four simulations were used to validate this model, including cube container with IP, sphere container with IP, cube container with non-overlapping spheres (i.e., PY), and sphere container with non-overlapping spheres. Once validated using simulations, the model can be used to predict structure function behavior for different model parameters, such as container size, shape, and pair correlation function.

The first two simulations were conducted assuming IP scattering with first a cube container and then a sphere container. A total of 10^4 scatterer positions inside the cube container having side length $L=1.0$ were selected randomly and independently. The simulation was repeated but for a sphere container with diameter $L=1.0$. Each coordinate for each scatterer position in 3D space was generated using a continuous uniform random number generator with range $[0, 1]$. For the spherical container, a scatterer position was discarded if it was outside of the sphere container and retained if it was inside the sphere container. The spacing between each scatterer position and every other scatterer position was computed. Using this collection of scatterer spacings, kernel density estimation was used to estimate the scatterer spacing probability distribution, $p(\Delta\mathbf{r})$. This simulation was repeated ten times using the IP pair correlation function $g(\Delta r) = 1$ and $W(\Delta\mathbf{r}) = W_{cube}(\Delta\mathbf{r})$ or $W_{sphere}(\Delta\mathbf{r})$, respectively.

The first two simulations were repeated using the PY structure function, i.e., non-overlapping spheres. Spherical scatterers having radius $a=0.05$ were placed in a cube or

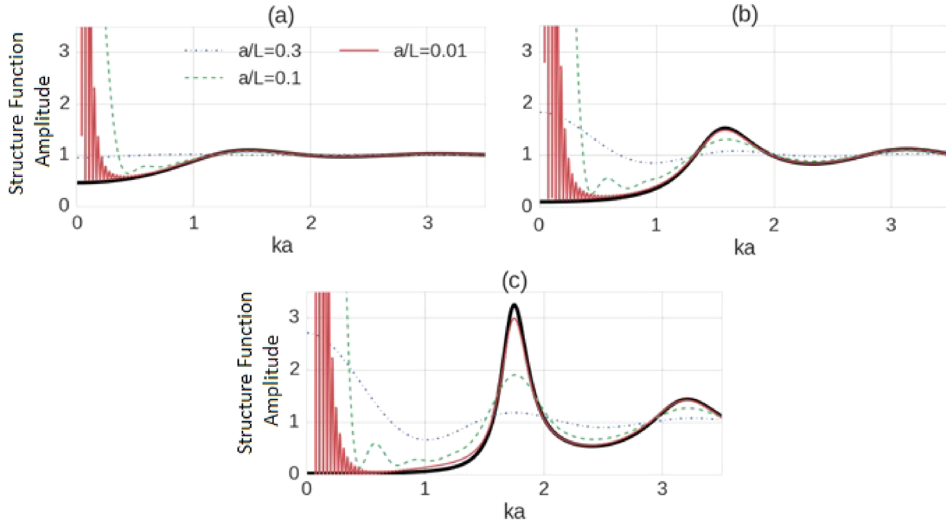


FIG. 6. (Color online) Example structure functions (unitless) assuming PY correlation function and a spherical container. The volume fraction was (a) 10%, (b) 30%, and (c) 50%. The thick black line is the PY structure function without a container.

spherical container using the Metropolis algorithm (Torquato, 2013). A total of 573 spheres were placed in the containers, both cube and spherical, for a volume fraction of 30%. For the spherical container, once the Metropolis algorithm stopped, the scatterer positions outside a sphere having diameter $L = 1.0$ were discarded. The simulation produced a set of scatterer positions associated with each of the spherical scatterers in the volume. The spacing between each scatterer position and every other scatterer position was computed. This simulation was repeated 1000 times and the collection of scatterer spacing probability distributions were averaged.

B. 2DZM analysis of high scatterer density media

The next set of simulations were conducted to demonstrate that the 2DZM method also works for media with correlation coefficients and power spectra that depend on the size and shape of the scatterers, but also the 3D positions of the scatterers. The simulations consisted of dense collections of spheres having volume fraction 30%. The theoretical correlation coefficient and power spectrum for this random process are shown in Fig. 7. For finite sized volumes, these curves result when averaging over many realizations. The correlation coefficient for dense collections of monodisperse spheres in Fig. 7(a) exhibits structure that depends on the 3D positions of the scatterers. Similar structure is exhibited for the power spectrum.

A total of 50 cube container volumes with side length $L = 1.0$ were filled with spherical scatterers having radius $a = 0.02$ and a volume fraction of 30%. The Metropolis algorithm was used to place the spheres so that they did not overlap. The 3D volume grid was sampled at 2^8 points along each dimension for a total of 2^{24} sampling points.

To study the bias in the estimated correlation coefficients and power spectra, the variance was eliminated by averaging large numbers of 2DZMs. Specifically, the correlation coefficient was estimated from all available 2DZMs in these simulations such that a total of $256 \times 50 = 12800$ 2DZMs were used to estimate the correlation coefficient. Four different 2DZM sizes were studied, where the size of

the 2DZM was specified by its side length L . The examined 2DZM sizes included $L = 0.0625$, $L = 0.125$, $L = 0.25$, and $L = 0.5$.

IV. RESULTS

A. Structure function versus container model

Cross-sectional views of the scatterer spacing distribution $p(\Delta\mathbf{r})$ for IP assuming a cube container for model and simulation are provided in Figs. 8(a) and 8(c), respectively. When using a sphere container, the resulting cross-sectional views for model and simulation are shown in Figs. 8(b) and 8(d), respectively. The error between the modeled and simulated distributions was calculated as

$$\text{error} = p_{\text{model}}(\Delta r) - p_{\text{sim}}(\Delta r). \quad (18)$$

The error between the model and simulation scatterer spacing probability distribution is shown in Fig. 9. The root-mean-square error (RMSE) was found between the model and simulation probability distributions (Fig. 10). The error in the simulated scatterer spacing probability distribution depends on the number of scatterer spacings used to estimate the scatterer spacing probability distribution. Therefore, the RMSE is a function of the number of scatterer spacings included in the analysis. If the modeled probability distribution is correct, the simulated probability distribution RMSE should converge to zero as the number of scatterer spacings in the analysis increases.

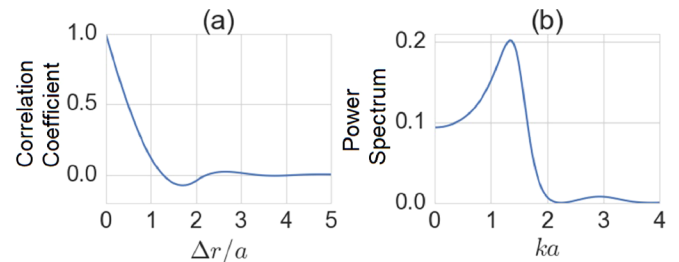


FIG. 7. (Color online) (a) Correlation coefficient and (b) power spectrum for a collection of dense monodisperse spheres with volume fraction 30%.

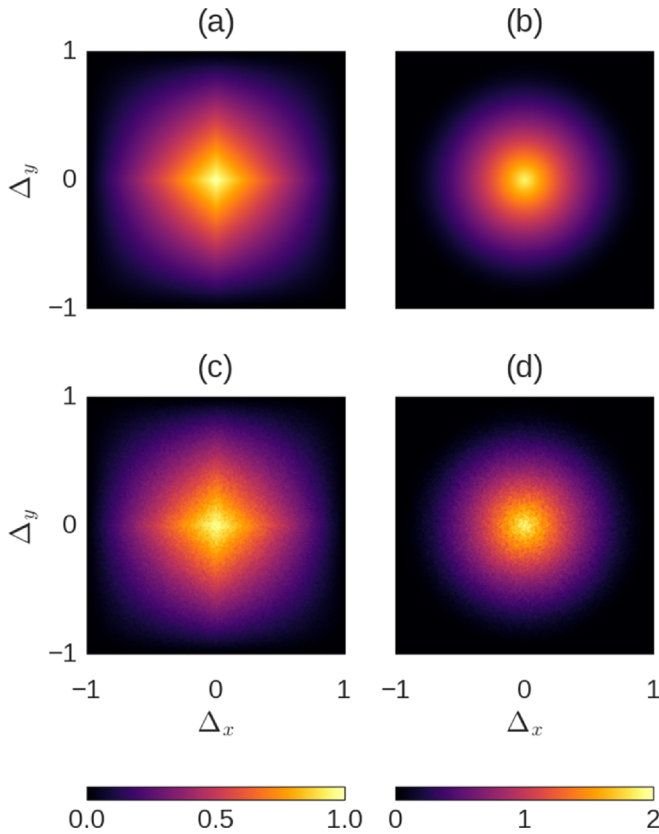


FIG. 8. (Color online) Example cross sections from the scatterer spacing probability distribution assuming IP. Modeled probability distributions for the (a) cube and (b) sphere containers. Estimated probability distributions for the (c) cube and (d) sphere containers. The cube container had side length $L = 1.0$ and the sphere container had diameter $L = 1.0$.

Examples of cross sections of the scatterer spacing distribution $p(\Delta\mathbf{r})$ for the PY pair correlation function assuming a cube container for the model and simulation are shown in Figs. 11(a) and 11(c), respectively. When using a sphere container, resulting example cross sections for model and simulation are in Figs. 11(b) and 11(d), respectively. The error between the model and simulation scatterer spacing probability distribution is shown in Fig. 12. The RMSE

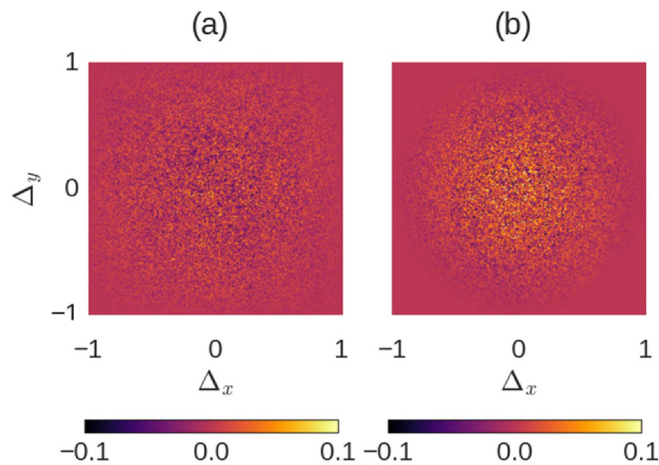


FIG. 9. (Color online) Error between modeled and simulated scatterer spacing probability distributions for (a) cube and (b) spherical containers assuming the IP pair correlation function.

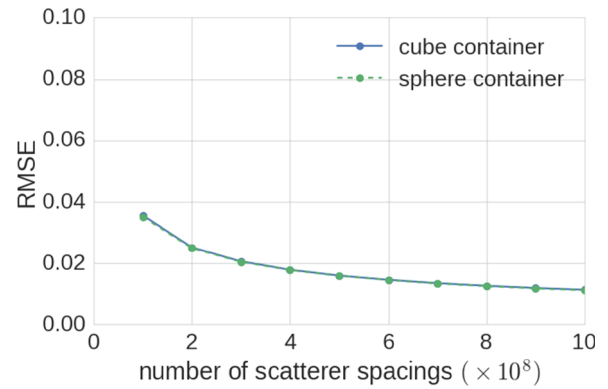


FIG. 10. (Color online) RMSE between modeled and simulated scatterer spacing probability distributions for cube and spherical containers assuming the IP pair correlation function. The RMSE is given as a function of the number of scatterer spacings included in the simulation analysis. The number of scatterer spacings can be increased by including more spheres in the simulation or by averaging results from independent simulations.

between model and simulation is shown as a function of the number of scatterer spacings included in the simulation in Fig. 13.

B. 2DZM analysis of high scatterer density media

The estimated correlation coefficient and power spectrum for each of the studied 2DZM sizes are shown in Fig. 14.

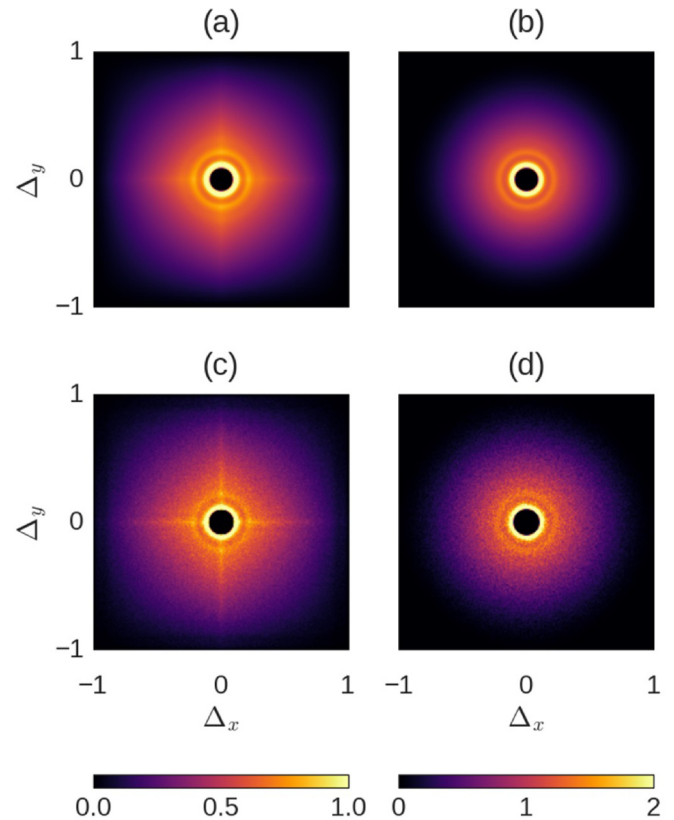


FIG. 11. (Color online) Example cross sections from the scatterer spacing probability distribution assuming PY. Modeled probability distributions for the (a) cube and (b) sphere containers. Estimated probability distributions for the (c) cube and (d) sphere containers. The cube container had side length $L = 1.0$ and the sphere container had diameter $L = 1.0$. The spherical scattering objects had radius $a = 0.05$.

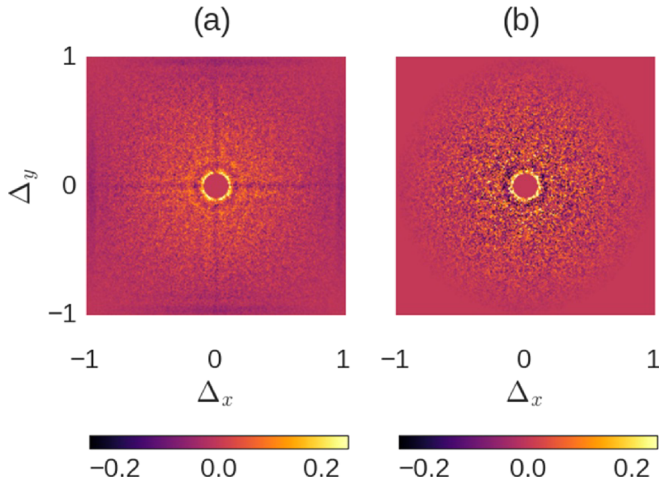


FIG. 12. (Color online) Error between modeled and simulated scatterer spacing probability distributions for (a) cube and (b) spherical containers assuming the PY pair correlation function.

The RMSE between estimated and theoretical correlation coefficients and the RMSE between estimated and theoretical power spectra for the different sized 2DZMs are shown in Fig. 15. The previous study results established that 2DZM analysis can capture information about the 3D size and shape of scatterers (Luchies and Oelze, 2016). The results in Fig. 14 are important because they demonstrate that 2DZMs can also capture information about the 3D location of the scatterers. Excellent agreement was observed between the 2DZM estimated and theoretical correlation coefficients (RMSE: 0.2%) in Fig. 14 when using 2DZMs with size $L = 0.5$. Good agreement was observed in the case of the power spectrum (RMSE: 11%). Good agreement was observed between estimated and theoretical correlation coefficients (RMSE: 7.0%) using 2DZM size $L = 0.0625$. Poor agreement was observed for the power spectrum (RMSE: 150%) using this size 2DZM.

C. Discussion

For the IP and PY scatterer spacing probability distributions, visual inspection between the model and simulation results in Fig. 8 and Fig. 11 for the IP and PY distributions,

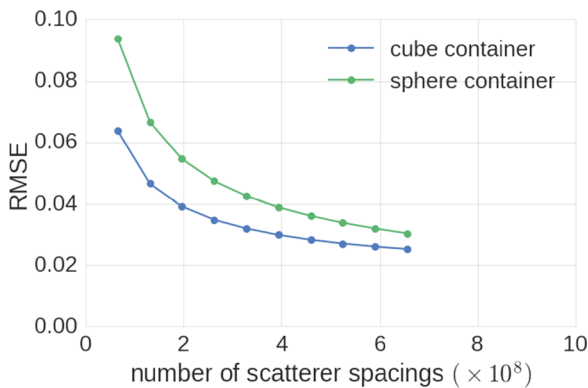


FIG. 13. (Color online) RMSE between modeled and simulated scatterer spacing probability distributions for cube and spherical containers assuming the PY pair correlation function. The RMSE is given as a function of the number of scatterer spacings included in the simulation analysis.

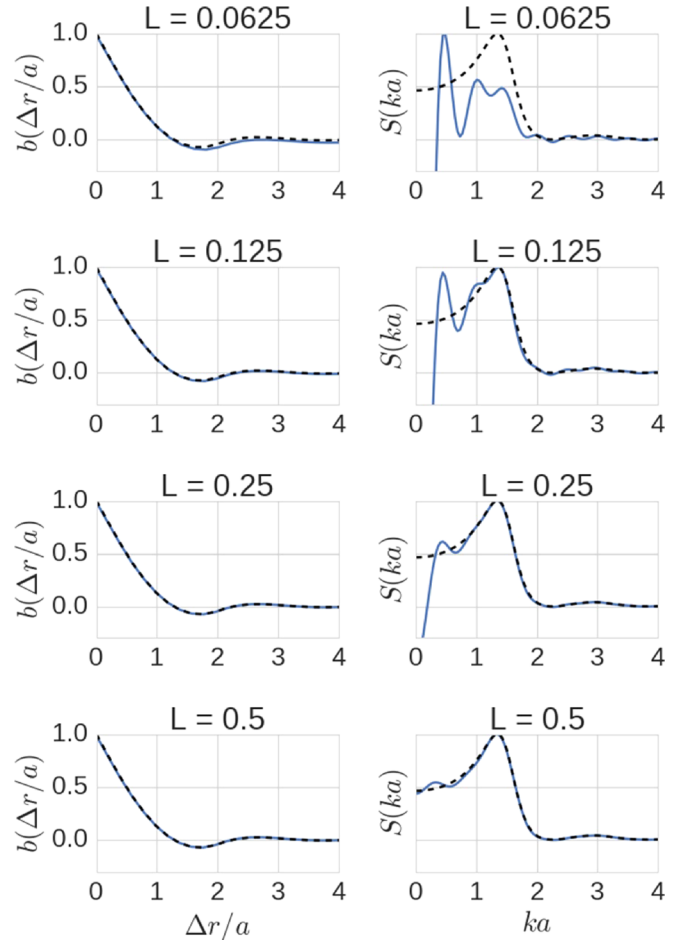


FIG. 14. (Color online) Estimated (left column) correlation coefficient and (right column) power spectrum for dense spheres with volume fraction 30% using 2DZMs with different sizes. The dashed line represents the theoretical prediction.

respectively, indicated good agreement for the cube and sphere containers. For IP, the error between model and simulation decreased as a function of the distance from the origin. The scatterer spacing distribution also decreased in this manner. However, for PY there were some discrepancies between model and simulation that appeared in Fig. 12. For the case of a cube container, discrepancies existed on-axis where the model probability distribution had magnitude value below the simulation probability distribution (i.e., a negative error value). In addition, for both cube and sphere containers, discrepancies existed between model and

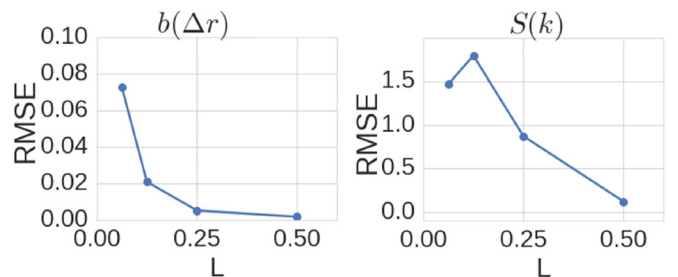


FIG. 15. (Color online) RMSE for estimated (left) correlation coefficients and (right) power spectra for dense spheres with volume fraction 30% using 2DZMs and different 2DZM sizes.

simulation near the scatterer spacing radial value $\Delta r = 2a$, where a is the radius of the spherical scatterers. The PY pair correlation function is an approximation for the pair correlation function produced by using an equilibrium method to fill a volume with non-overlapping spheres. Therefore, the error between the model and simulation may be due to this approximation. At the same time, RMSE curves between simulations and models, i.e., Figs. 10 and 13, were small indicating good agreement especially at high number of scatterer spacings.

The first set of simulations served as validation for the structure function with container effects. This model could be used to study the effect of a container on ZMs or the effect of a focal region and time gating on BSC estimation, which can also be thought of as derived from a container, i.e., the focal zone, with a finite number of scatterers contained within.

The dense sphere simulations (second set of simulations) were significant because they demonstrated that 2DZMs could capture information about the 3D spatial positions of the scatterers in addition to information about the size and shape of the scatterers. The simulations indicated that using too small a 2DZM resulted in biased correlation coefficient and power spectral estimates. The simulations demonstrated that the power spectral estimates were sensitive to small errors in the correlation coefficient estimate. These findings suggest that the correlation coefficient should be modeled instead of the power spectrum when conducting 2DZM analysis, especially when conducting analysis of dense media.

The results in Fig. 14 demonstrate the importance of using a 2DZM having sufficient size relative to the scatterer size. When a 2DZM size that was too small was used, the correlation coefficient and power spectral estimates were biased. The correlation coefficient was underestimated when using 2DZM size that was too small. The power spectrum exhibited negative values for small values of ka when the 2DZM size was too small. Therefore, when conducting 2DZM analysis, it is important to determine if a sufficiently sized 2DZM is being used.

The RMSE curves in Fig. 15 show that error decreased as the size of the 2DZM was increased. The error between the estimated and theoretical power spectra was larger than that between estimated and theoretical correlation coefficients. Because only small errors were observed in the estimated correlation coefficient, but larger errors were observed in the power spectrum, this result suggests that the power spectral estimate was sensitive to small errors in the correlation coefficient estimate. As previously indicated, this finding suggests that when conducting 2DZM analysis, it is better to analyze the correlation coefficient instead of the power spectrum.

The simulation analysis demonstrated that the correlation coefficient and power spectrum could be estimated for a dense collection of spheres using 2DZMs. Our previous study demonstrated that the 2DZM approach could correctly estimate correlation coefficients and power spectra for sparse media (Luchies and Oelze, 2016). The current finding is significant because it implies that 2DZMs can capture information about the 3D spatial positions of the scatterers in

addition to information about the size and shape of the scatterers for a dense scattering media, which is expected to be encountered in many tissues. Therefore, the utility of the 2DZM is much more applicable than to just sparse scattering media. Furthermore, the 2DZM approach captures the structure function contribution.

The results further indicated that increasing 2DZM size relative to the scatterer size reduced bias in the estimated correlation coefficient and power spectrum. The important quantity is the ratio L/a , where L is the 2DZM side length and a is the scatterer radius. The RMSE between estimated and theoretical correlation coefficients was 2.0% ($L/a = 6.25$), 0.5% ($L/a = 12.5$), and 0.1% ($L/a = 25$). The RMSE between the estimated and theoretical power spectra was 180% ($L/a = 6.25$), 87% ($L/a = 12.5$), and 11% ($L/a = 25$).

Several applications exist for the structure function with container effects. The model was developed to determine the effect of a container on ZM analysis. ZMs are usually confined to a cube, so the structure function with container effects model suggests that on-axis lines from the spectral estimates of a ZM be avoided or that a spherical container be used instead of a cube (in the case of a 2DZM a circular domain should be used instead of a square domain). The predictions of this model also apply to estimating BSCs from ultrasound signals. When estimating BSCs, there is a lateral cross-sectional area associated with the finite aperture of the source and an axial length associated with the length of the time gate used. These dimensions define a container that in the roughest approximation is a cylinder. By adjusting the focal properties of the source or the gate length used for analyzing the signal, the container can be manipulated. Using the proposed model, the effects of the container on the structure function could be studied and used to determine to what degree the container affects BSC estimates from ultrasound signals.

The final application is related to clustering of scatterers. Recent work has proposed using ultrasound to study the aggregation of red blood cells as an indicator of disease (Fontaine *et al.*, 1999; Franceschini *et al.*, 2010; Franceschini *et al.*, 2011; de Monchy *et al.*, 2016). In these studies, clusters of red blood cells are modeled as being an effective scatterer with new acoustic properties related to the cluster properties. For example, the effective scatterer might be a sphere or a cylinder. A structure function model is then applied to the effective scatterers to characterize the BSC from blood. The structure function with container could be applied at the level of individual clusters of red blood cells. A container such as a sphere could be assumed for the red blood cells and a structure function with container effects model applied to the collection of red blood cells confined to the sphere. A second structure function could then be assumed for the collection of scattering clusters. In this way, a hierarchical structure function model could be constructed to describe scattering by red blood cell aggregates.

In this work, we developed a structure function that incorporates the effects of confining scatterer positions to a finite container for dense scattering media and verified that a 2DZM analysis could be utilized in the case of dense media. Standard structure function analysis does not include this

constraint on scatterer positions. Instead, the assumption is usually made that the container is large enough so that container effects are not a problem. The developed structure function with container effects can be used to determine the ratio between scatterer size and container size such that container effects would distort the structure function assuming no container effects.

ACKNOWLEDGMENTS

This work was funded in part by a grant from the National Institutes of Health (Grant No. EB020766).

- Anderson, V. C. (1950). "Sound scattering from a fluid sphere," *J. Acoust. Soc. Am.* **22**(4), 426–431.
- Chen, X., Phillips, D., Schwarz, K. Q., Mottley, J. G., and Parker, K. J. (1997). "The measurement of backscatter coefficient from a broadband pulse-echo system: A new formulation," *IEEE Trans. Ultrason. Ferroelectr. Freq. Control* **44**, 515–525.
- Czarnota, G. J., Kolios, M. C., Abraham, J., Portnoy, M., Ottensmeyer, M., Hunt, J., and Sherar, M. (1999). "Ultrasound imaging of apoptosis: High-resolution non-invasive monitoring of programmed cell death in vitro, in situ and in vivo," *Br. J. Cancer* **81**, 520–527.
- de Monchy, R., Destrempes, F., Saha, R. K., Cloutier, G., and Franceschini, E. (2016). "Coherent and incoherent ultrasound backscatter from cell aggregates," *J. Acoust. Soc. Amer.* **140**, 2173–2184.
- Feleppa, E. J., Kalisz, A., Sokil-Melgar, J., Lizzi, F., Liu, T., Rosado, A., Shao, M., Fair, W., Wang, Y., and Cookson, M. (1996). "Typing of prostate tissue by ultrasonic spectrum analysis," *IEEE Trans. Ultrason. Ferroelectr. Freq. Control* **43**, 609–619.
- Feleppa, E. J., Lizzi, F. L., Coleman, D. J., and Yaremko, M. M. (1986). "Diagnostic spectrum analysis in ophthalmology: A physical perspective," *Ultrasound Med. Biol.* **12**, 623–631.
- Fellingham, L. L., and Sommer, F. G. (1984). "Ultrasonic characterization of tissue structure in the in vivo human liver and spleen," *IEEE Trans. Son. Ultrason.* **31**, 418–428.
- Fontaine, I., Bertrand, M., and Cloutier, G. (1999). "A system-based approach to modeling the ultrasound signal backscattered by red blood cells," *Biophys. J.* **77**, 2387–2399.
- Franceschini, E., Francois, T., Destrempes, F., and Cloutier, G. (2010). "Ultrasound characterization of red blood cell aggregation with intervening attenuating tissue-mimicking phantoms," *J. Acoust. Soc. Am.* **127**, 1104–1115.
- Franceschini, E., Metzger, B., and Cloutier, G. (2011). "Forward problem study of an effective medium model for ultrasound blood characterization," *IEEE Trans. Ultrason. Ferroelectr. Freq. Control* **58**, 2668–2679.
- Han, A., and O'Brien, W. D., Jr. (2015). "Structure function for high concentration biophantoms of polydisperse scatterer sizes," *IEEE Trans. Ultrason. Ferroelectr. Freq. Control* **62**, 303–318.
- Insana, M. F. (1995). "Modeling acoustic backscatter from kidney microstructure using an anisotropic correlation function," *J. Acoust. Soc. Am.* **97**, 649–655.
- Insana, M. F., and Brown, D. G. (1992). "Acoustic scattering theory applied to soft biological tissues," in *Ultrasonic Scattering in Biological Tissues*, edited by K. K. Shung and G. A. Thieme (CRC Press, Boca Raton, FL), pp. 75–124.
- Insana, M. F., Wagner, R. F., Brown, D. G., and Hall, T. J. (1990). "Describing small-scale structure in random media using pulse-echo ultrasound," *J. Acoust. Soc. Am.* **87**, 179–192.
- Lavarello, R. J., Ghoshal, G., and Oelze, M. L. (2011). "On the estimation of backscatter coefficients using single-element focused transducers," *J. Acoust. Soc. Am.* **129**, 2903–2911.
- Luchies, A. C. (2016). "Using two-dimensional impedance maps to study acoustic properties of tissue microstructure," Ph.D. dissertation, University of Illinois, Champaign, IL.
- Luchies, A. C., and Oelze, M. L. (2013). "Modeling volume power spectra for collections of spheres in a finite container," in *Proceedings of the 2013 Joint UFFC, EFTF and PFM Symposium*, July 21–25, Prague, Czech Republic, pp. 413–416.
- Luchies, A. C., and Oelze, M. L. (2016). "Using two-dimensional impedance maps to study weak scattering in sparse random media," *J. Acoust. Soc. Am.* **139**, 1557–1564.
- Mamou, J., Coron, A., Oelze, M. L., Saegusa-Becroft, E., Hata, M., Lee, P., Machi, J., Yanagihara, E., Laugier, P., and Feleppa, E. J. (2011). "Three-dimensional high-frequency backscatter and envelope quantification of cancerous human lymph nodes," *Ultrasound Med. Biol.* **37**, 345–357.
- Mamou, J., Oelze, M. L., O'Brien, W. D., Jr., and Zachary, J. F. (2005). "Identifying ultrasonic scattering sites from three-dimensional impedance maps," *J. Acoust. Soc. Am.* **117**, 413–423.
- Mamou, J., Oelze, M. L., O'Brien, W. D., Jr., and Zachary, J. F. (2008). "Extended three-dimensional impedance map methods for identifying ultrasonic scattering sites," *J. Acoust. Soc. Am.* **123**, 1195–1208.
- McNew, J., Lavarello, R., and O'Brien, W. D., Jr. (2009). "Sound scattering from two concentric fluid spheres," *J. Acoust. Soc. Am.* **125**, 1–4.
- Morse, P. M., and Ingard, K. U. (1968). *Theoretical Acoustics* (McGraw-Hill, New York).
- Oelze, M. L., O'Brien, W. D., Jr., Blue, J. P., and Zachary, J. F. (2004). "Differentiation and characterization of rat mammary fibroadenomas and 4T1 mouse carcinomas using quantitative ultrasound imaging," *IEEE Trans. Med. Imaging* **23**, 764–771.
- Percus, J. K., and Yevick, G. J. (1958). "Analysis of classical statistical mechanics by means of collective coordinates," *Phys. Rev.* **110**, 1–13.
- Tamirisa, P. K., Holland, M. R., Miller, J. G., and Perez, J. E. (2001). "Ultrasonic tissue characterization: Review of an approach to assess hypertrophic myocardium," *Echocardiography* **18**, 593–597.
- Torquato, S. (2013). *Random Heterogeneous Materials: Microstructure and Macroscopic Properties* (Springer, New York).
- Twersky, V. (1987). "Low-frequency scattering by correlated distributions of randomly oriented particles," *J. Acoust. Soc. Am.* **81**, 1609–1618.
- Ueda, M., and Ozawa, Y. (1985). "Spectral analysis of echoes for backscattering coefficient measurement," *J. Acoust. Soc. Am.* **77**, 38–47.
- Vlad, R. M., Brand, S., Giles, A., Kolios, M. C., and Czarnota, G. J. (2009). "Quantitative ultrasound characterization of responses to radiotherapy in cancer mouse models," *Clin. Cancer Res.* **15**, 2067–2075.
- Widom, B. (1966). "Random sequential addition of hard spheres to a volume," *J. Chem. Phys.* **44**, 3888–3894.